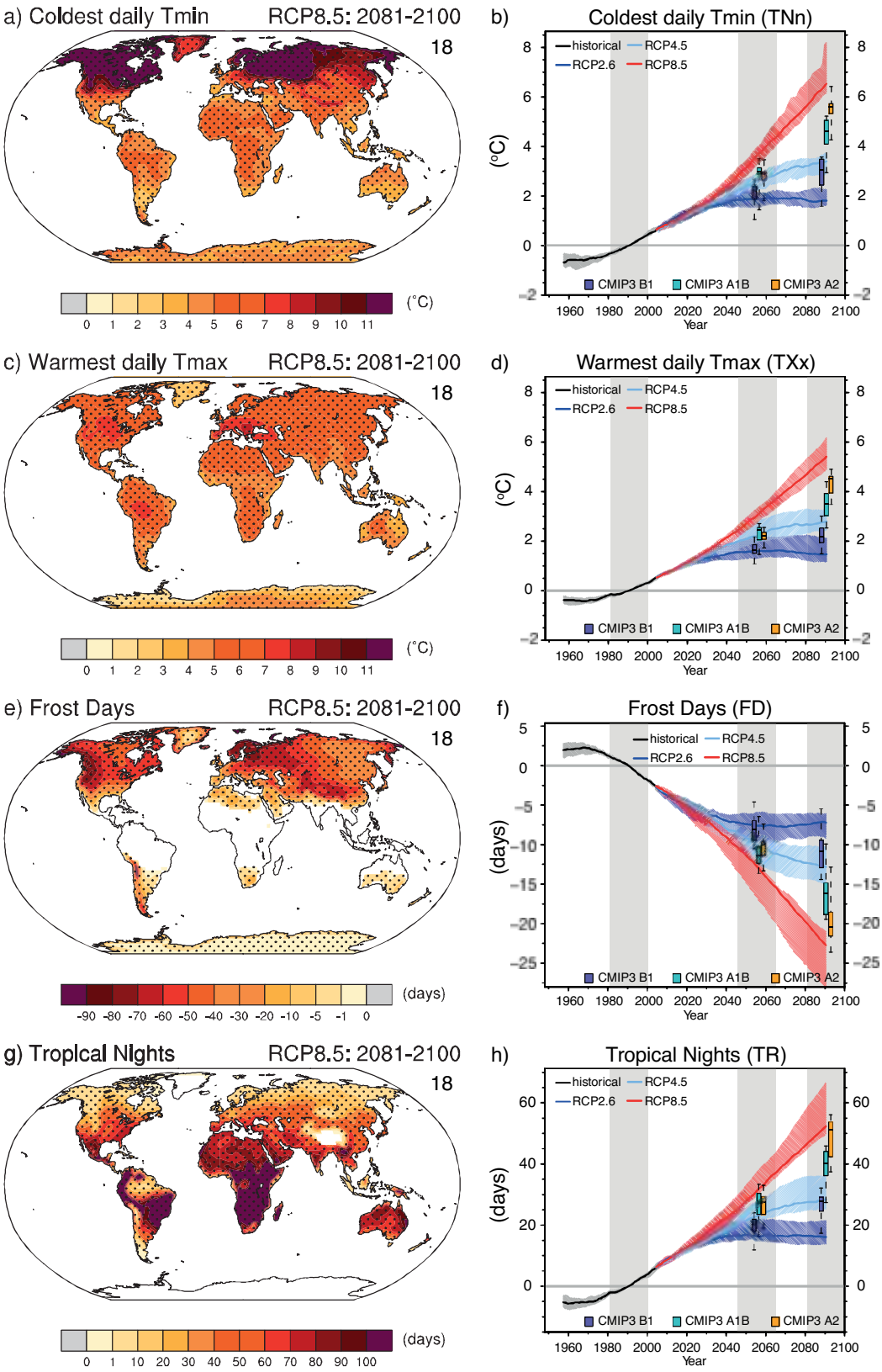

Figure 12.13 | CMIP5 multi-model mean geographical changes (relative to a 1981–2000 reference period in common with CMIP3) under RCP8.5 and 20-year smoothed time series for RCP2.6, RCP4.5 and RCP8.5 in the (a, b) annual minimum of daily minimum temperature, (c, d) annual maximum of daily maximum temperature, (e, f) frost days (number of days below 0°C) and (g, h) tropical nights (number of days above 20°C). White areas over land indicate regions where the index is not valid. Shading in the time series represents the interquartile ensemble spread (25th and 75th quantiles). The box-and-whisker plots show the interquartile ensemble spread (box) and outliers (whiskers) for 11 CMIP3 model simulations of the SRES scenarios A2 (orange), A1B (cyan), and B1 (purple) globally averaged over the respective future time periods (2046–2065 and 2081–2100) as anomalies from the 1981–2000 reference period. Stippling indicates grid points with changes that are significant at the 5% level using a Wilcoxon signed-ranked test. (Updated from Sillmann et al. (2013), excluding the FGOALS-s2 model.)

winter mean temperature changes, particularly over parts of North America and Europe. Kharin et al. (2013) concluded from the CMIP5 models that it is *likely* that in most land regions a current 20 year maximum temperature event is projected to become a one-in-two-year event by the end of the 21st century under the RCP4.5 and RCP8.5 scenarios, except for some regions of the high latitudes of the NH where it is *likely* to become a one-in-five-year event (see also Seneviratne et al. (2012) Figure 3.5). Current 20-year minimum temperature events are projected to become exceedingly rare, with return periods *likely* increasing to more than 100 years in almost all locations under RCP8.5 (Kharin et al., 2013). Section 10.6.1.1 notes that a number of detection and attribution studies since SREX suggest that the model changes may tend to be too large for warm extremes and too small for cold extremes and thus these likelihood statements are somewhat less strongly stated than a direct interpretation of model output and its ranges. The CMIP5 analysis shown in Figure 12.14 reinforces this assessment of large changes in the frequency of rare events, particularly in the RCP8.5 scenario (Kharin et al., 2013).

There is high consensus among models in the sign of the future change in temperature extremes, with recent studies confirming this conclusion from the previous assessments (Tebaldi et al., 2006; Meehl et al., 2007b; Orlowsky and Seneviratne, 2012; Seneviratne et al., 2012; Sillmann et al., 2013). However, the magnitude of the change remains uncertain owing to scenario and model (both structural and parameter) uncertainty (Clark et al., 2010) as well as internal variability. These uncertainties are much larger than corresponding uncertainties in the magnitude of mean temperature change (Barnett et al., 2006; Clark et al., 2006; Fischer and Schär, 2010; Fischer et al., 2011).

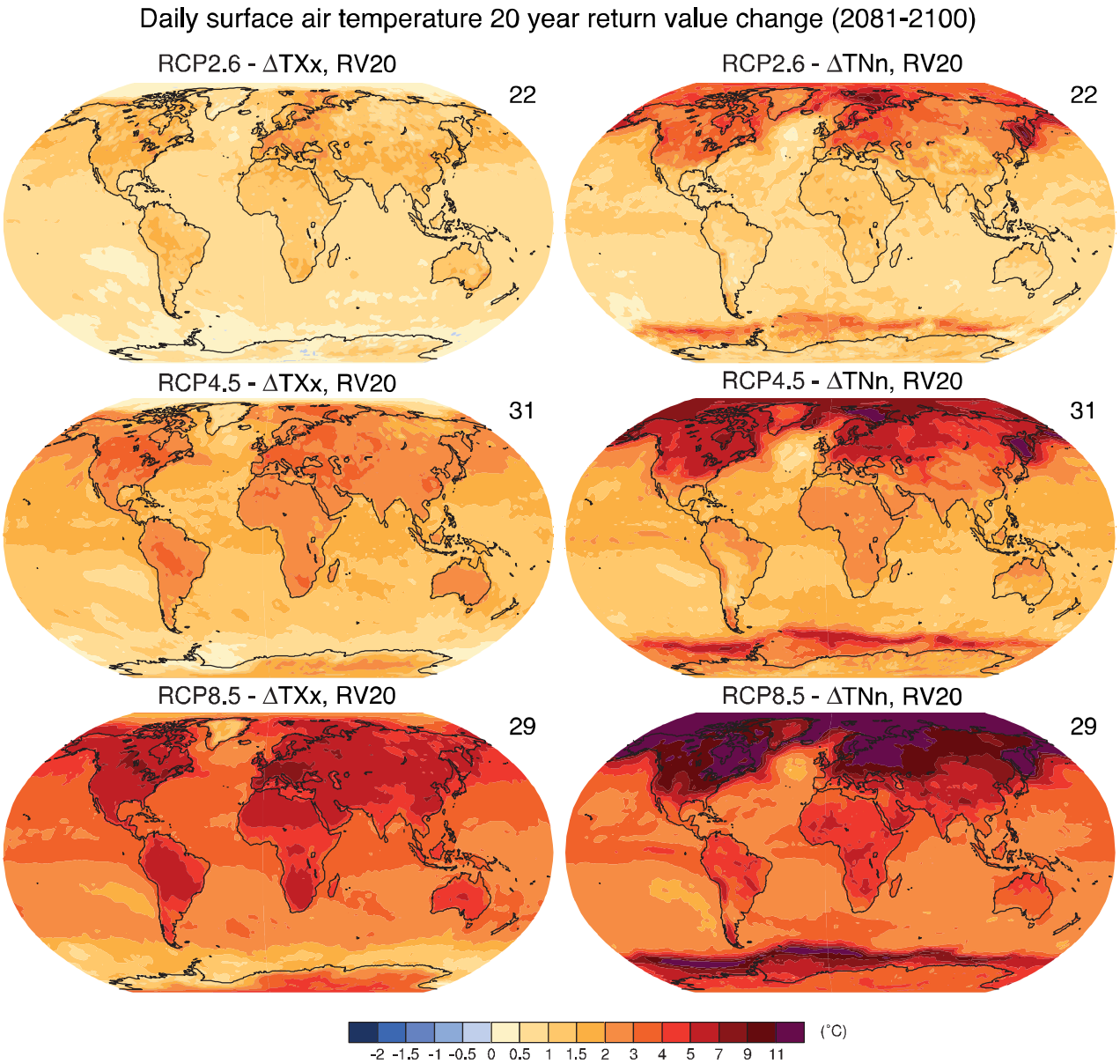

Figure 12.14 | The CMIP5 multi-model median change in 20-year return values of annual warm temperature extremes (left-hand panels) and cold temperature extremes (right-hand panels) as simulated by CMIP5 models in 2081–2100 relative to 1986–2005 in the RCP2.6 (top), RCP4.5 (middle panels), and RCP8.5 (bottom) experiments.

LW radiation. The LW net flux depends mainly on two factors: the surface temperature and the magnitude of the greenhouse effect of the atmosphere. During the 20th century, the rapid fluctuations of LW radiation are driven by volcanic forcings, which decrease the absorbed SW radiation, surface temperature, and the LW radiation emitted by the Earth toward space. During the period 1960–2000, the fast increase of GHG concentrations also decreases the radiation emitted by the Earth. In response to this net heating of the Earth, temperatures warm and thereby increase emitted LW radiation although the change of the temperature vertical profile, water vapour, and cloud properties modulate this response (e.g., Bony et al., 2006; Randall et al., 2007).

12.4.3.5 Clouds

This section provides a summary description of future changes in clouds and their feedbacks on climate. A more general and more precise description and assessment of the role of clouds in the climate system is provided in Chapter 7, in particular Section 7.2 for cloud processes and feedbacks and Section 7.4 for aerosol–cloud interactions. Cloud feedbacks and adjustments are presented in Section 7.2.5 and a synthesis is provided in Section 7.2.6. Clouds are a major component of the climate system and play an important role in climate sensitivity (Cess et al., 1990; Randall et al., 2007), the diurnal temperature range (DTR) over land (Zhou et al., 2009), and land–sea contrast (see Section 12.4.3.1). The observed global mean cloud RF is about –20 W m^{-2} (Loeb et al., 2009) (see Section 7.2.1), that is, clouds have a net cooling effect. Current GCMs simulate clouds through various complex parameterizations (see Section 7.2.3), and cloud feedback is a major source of the spread of the climate sensitivity estimate (Soden and Held, 2006; Randall et al., 2007; Dufresne and Bony, 2008) (see Section 9.7.2).

Under future projections the multi-model pattern of total cloud amount shows consistent decreases in the subtropics, in conjunction with a decrease of the relative humidity there, and increases at high latitudes. Another robust pattern is an increase in cloud cover at all latitudes in the vicinity of the tropopause, a signature of the increase of the altitude of high level clouds in convective regions (Wetherald and Manabe, 1988; Meehl et al., 2007b; Soden and Vecchi, 2011; Zelinka et al., 2012). Low-level clouds were identified as a primary cause of inter-model spread in cloud feedbacks in CMIP3 models (Bony and Dufresne, 2005; Webb et al., 2006; Wyant et al., 2006). Since AR4, these results have been confirmed along with the positive feedbacks due to high level clouds in the CMIP3 or CFMIP models (Zelinka and Hartmann, 2010; Soden and Vecchi, 2011; Webb et al., 2013) and CMIP5 models (Vial et al., 2013). Since AR4, the response of clouds has been partitioned in a direct or 'rapid' response of clouds to CO_2 and a 'slow' response of clouds to the surface temperature increase (i.e., the usual feedback response) (Gregory and Webb, 2008). The radiative effect of clouds depends mainly on their fraction, optical depth and temperature. The contribution of these variables to the cloud feedback has been quantified for the multi-model CMIP3 (Soden and Vecchi, 2011) and CFMIP1 database (Zelinka et al., 2012). These findings are consistent with the radiative changes obtained with the CMIP5 models (Figure 12.16) and may be summarized as follows (see Section 7.2.5 for more details).

The dominant contributor to the SW cloud feedback is the change in cloud fraction. The reduction of cloud fraction between 50°S and 50°N, except along the equator and the eastern part of the ocean basins (Figure 12.17), contributes to an increase in the absorbed solar radiation (Figure 12.16c). Physical mechanisms and the role of different parameterizations have been proposed to explain this reduction of low-level clouds (Zhang and Bretherton, 2008; Caldwell and Bretherton, 2009; Brient and Bony, 2013; Webb et al., 2013). Poleward of 50°S, the cloud fraction and the cloud optical depth increases, thereby increasing cloud reflectance. This leads to a decrease of solar absorption around Antarctica where the ocean is nearly ice free in summer (Figure 12.16c). However, there is *low confidence* in this result because GCMs do not reproduce the nearly 100% cloud cover observed there and the negative feedback could be overestimated (Trenberth and Fasullo, 2010) or, at the opposite, underestimated because the cloud optical depth simulated by models is biased high there (Zelinka et al., 2012).

In the LW domain, the tropical high cloud changes exert the dominant effect. A lifting of the cloud top with warming is simulated consistently across models (Meehl et al., 2007b) which leads to a positive feedback whereby the LW emissions from high clouds decrease as they cool (Figure 12.16b). The dominant driver of this effect is the increase of tropopause height and physical explanations have been proposed (Hartmann and Larson, 2002; Lorenz and DeWeaver, 2007; Zelinka

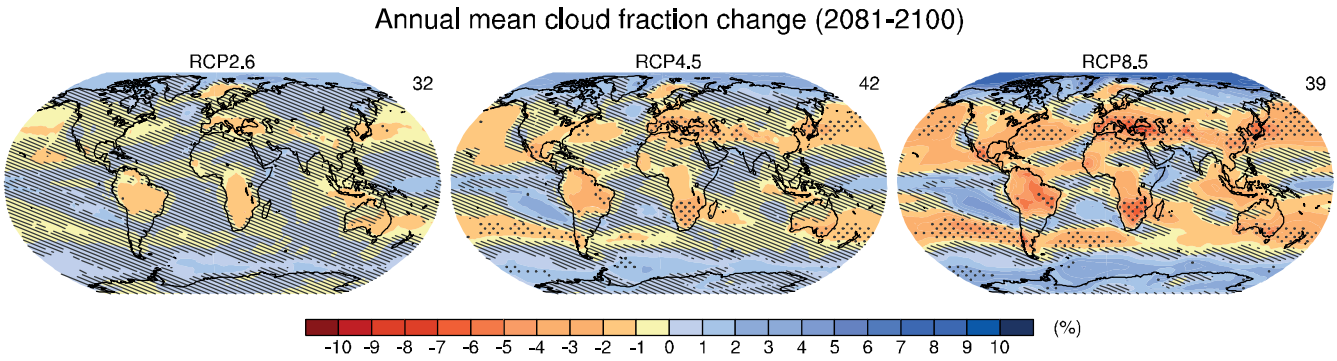

Figure 12.17 | CMIP5 multi-model changes in annual mean total cloud fraction (in %) relative to 1986–2005 for 2081–2100 under the RCP2.6 (left), RCP4.5 (centre) and RCP8.5 (right) forcing scenarios. Hatching indicates regions where the multi-model mean change is less than one standard deviation of internal variability. Stippling indicates regions where the multi-model mean change is greater than two standard deviations of internal variability and where 90% of the models agree on the sign of change (see Box 12.1). The number of CMIP5 models used is indicated in the upper right corner of each panel.

and Hartmann, 2010). Although the decrease in cloudiness generally increases outgoing longwave radiation and partly offsets the effect of cloud rising, the net effect is a consistent positive global mean LW cloud feedback across CMIP and CFMIP models. Global mean SW cloud feedbacks range from slightly negative to strongly positive (Soden and Vecchi, 2011; Zelinka et al., 2012), with an inter-model spread in net cloud feedback being mainly attributable to low-level cloud changes.

In summary, both the multi-model mean and the inter-model spread of the cloud fraction and radiative flux changes simulated by the CMIP5 models are consistent with those previously obtained by the CMIP3 models. These include decreases in cloud amount in the subtropics, increases at high latitudes and increases in the altitude of high level clouds in convective regions. Many of these changes have been understood primarily as responses to large-scale circulation changes (see Section 7.2.6).

12.4.4 Changes in Atmospheric Circulation

Projected changes in energy and water cycles couple with changes in atmospheric circulation and mass distribution. Understanding this coupling is necessary to assess physical behaviour underlying projected changes, particularly at regional scales, revealing why changes occur and the realism of the changes. The focus in this section is on atmospheric circulation behaviour that CMIP5 GCMs resolve well. Thus, the section includes discussion of extratropical cyclones but not tropical cyclones: extratropical cyclones are fairly well resolved by most CMIP5 GCMs, whereas tropical cyclones are not, requiring resolutions finer than used by the large majority of CMIP5 GCMs (see Section 9.5.4.3). Detailed discussion of tropical cyclones appears in Section 14.6.1 (see also Section 11.3.2.5.3 for near term changes and Section 3.4.4 in Seneviratne et al. (2012)). Regional detail concerning extratropical storm tracks, including causal processes, appears in Section 14.6.2 (see also Section 11.3.2.4 for near-term changes and Seneviratne et al. (2012) for an assessment of projected changes related to weather and climate extremes).

12.4.4.1 Mean Sea Level Pressure and Upper-Air Winds

Sea level pressure gives an indication of surface changes in atmospheric circulation (Figure 12.18). As in previous assessments, a robust feature of the pattern of change is a decrease in high latitudes and increases in the mid-latitudes, associated with poleward shifts in the SH mid-latitude storm tracks (Section 12.4.4.3) and positive trends in the annular modes (Section 14.5) as well as an expansion of the Hadley Cell (Section 12.4.4.2). Similar patterns of sea level pressure change are found in observed trends over recent decades, suggesting an already detectable change (Gillett and Stott, 2009; Section 10.3.3.4), although the observed patterns are influenced by both natural and anthropogenic forcing as well as internal variability and the relative importance of these influences is likely to change in the future. Internal variability has been found to play a large role in uncertainties of future sea level pressure projections, particularly at higher latitudes (Deser et al., 2012a).

In boreal winter, decreases of sea level pressure over NH high latitudes are slightly weaker in the CMIP5 ensemble compared to previous assessments, consistent with Scaife et al. (2012) and Karpechko and Manzini (2012), who suggest that improvements in the representation of the stratosphere can influence this pattern. In austral summer, the SH projections are impacted by the additional influence of stratospheric ozone recovery (see Section 11.3.2.4.2) which opposes changes due to GHGs. Under the weaker GHG emissions of RCP2.6, decreases in sea level pressure over the SH mid-latitudes and increases over SH high latitudes are consistent with expected changes from ozone recovery (Arblaster et al., 2011; McLandress et al., 2011; Polvani et al., 2011). For

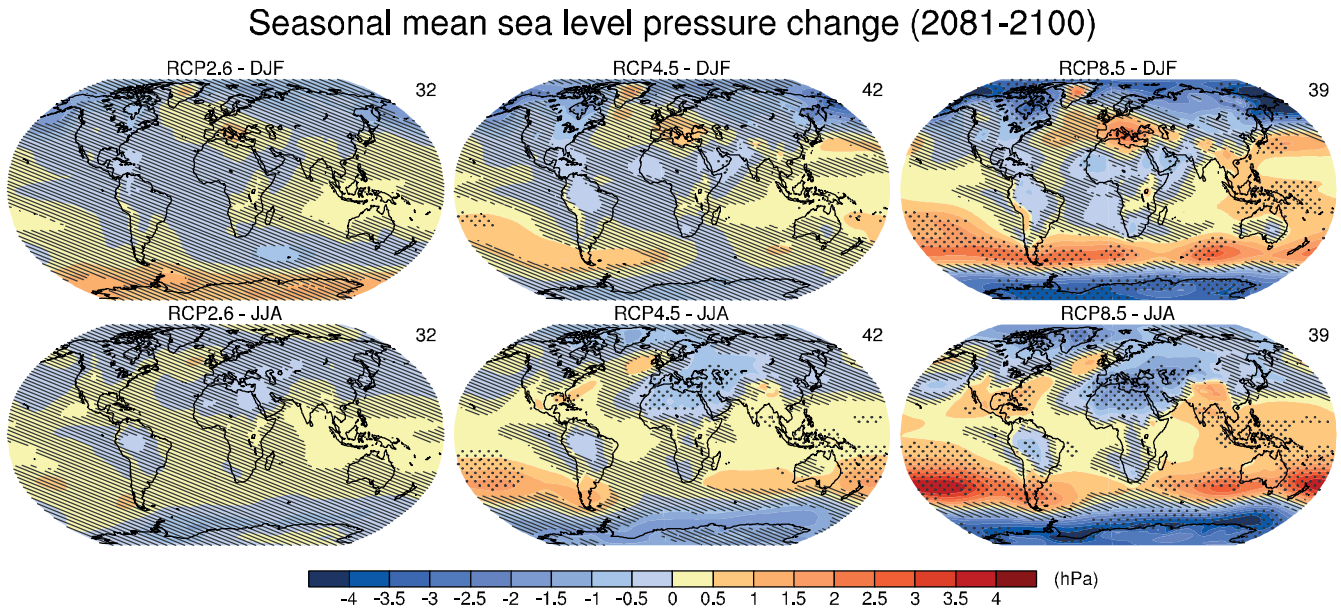

Figure 12.18 | CMIP5 multi-model ensemble average of December, January and February (DJF, top row) and June, July and August (JJA, bottom row) mean sea level pressure change (2081–2100 minus 1986–2005) for, from left to right, RCP2.6, 4.5 and 8.5. Hatching indicates regions where the multi-model mean change is less than one standard deviation of internal variability. Stippling indicates regions where the multi-model mean change is greater than two standard deviations of internal variability and where at least 90% of models agree on the sign of change (see Box 12.1).

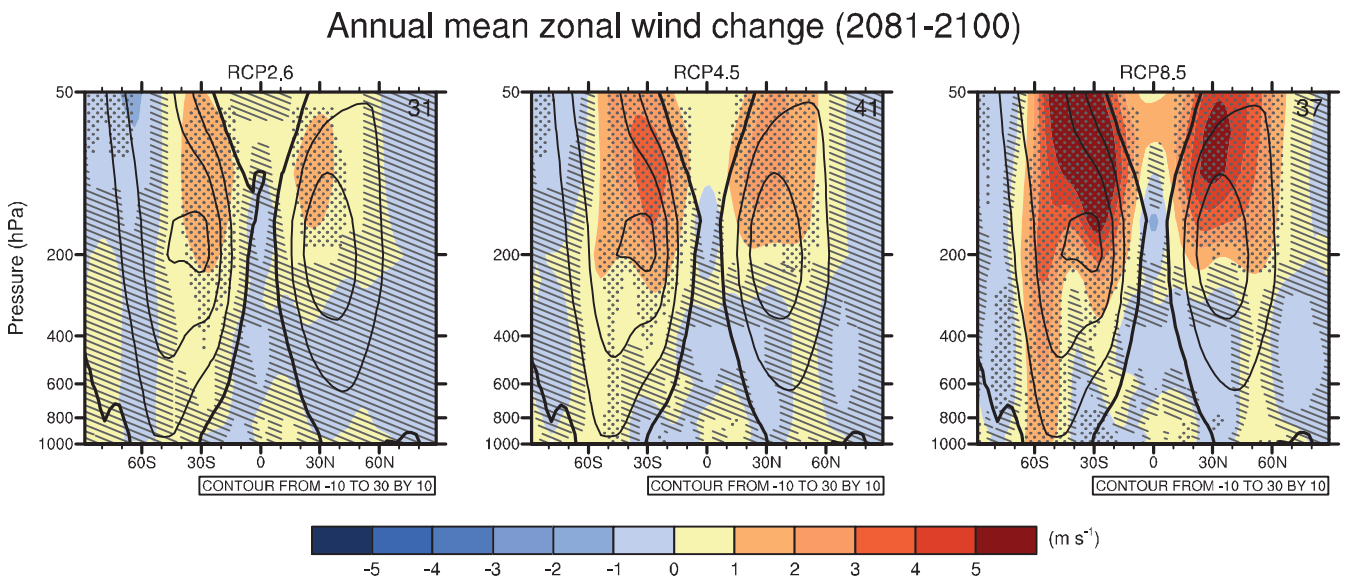

Figure 12.19 | Coupled Model Intercomparison Project Phase 5 (CMIP5) multi-model ensemble average of zonal and annual mean wind change (2081–2100 minus 1986–2005) for, from left to right, Representative Concentration Pathway 2.6 (RCP2.6), 4.5 and 8.5. Black contours represent the multi-model average for the 1986–2005 base period. Hatching indicates regions where the multi-model mean change is less than one standard deviation of internal variability. Stippling indicates regions where the multi-model mean change is greater than two standard deviations of internal variability and where at least 90% of models agree on the sign of change (see Box 12.1).

all other RCPs, the magnitude of SH extratropical changes scales with the RF, as found in previous model ensembles (Paeth and Pollinger, 2010; Simpkins and Karpechko, 2012).

Large increases in seasonal sea level pressure are also found in regions of sub-tropical drying such as the Mediterranean and northern Africa in DJF and Australia in JJA. Projected changes in the tropics are less consistent across the models; however, a decrease in the eastern equatorial Pacific and increase over the maritime continent, associated with a weakening of the Walker Circulation (Vecchi and Soden, 2007; Power and Kociuba, 2011b), is found in all RCPs.

Future changes in zonal and annual mean zonal winds (Figure 12.19) are seen throughout the atmosphere with stronger changes in higher RCPs. Large increases in winds are evident in the tropical stratosphere and a poleward shift and intensification of the SH tropospheric jet is seen under RCP4.5 and RCP8.5, associated with an increase in the SH upper tropospheric meridional temperature gradient (Figure 12.12) (Wilcox et al., 2012). In the NH, the response of the tropospheric jet is weaker and complicated by the additional thermal forcing of polar amplification (Woollings, 2008). Barnes and Polvani (2013) evaluate changes in the annual mean mid-latitude jets in the CMIP5 ensemble, finding consistent poleward shifts in both hemispheres under RCP8.5 for the end of the 21st century. In the NH, the poleward shift is ~1°, similar to that found for the CMIP3 ensemble (Woollings and Blackburn, 2012). In the SH, the annual mean mid-latitude jet shifts poleward by ~2° under RCP8.5 at the end of the 21st century in the CMIP5 multi-model mean (Barnes and Polvani, 2013), with a similar shift of 1.5° in the surface westerlies (Swart and Fyfe, 2012). A strengthening of the SH surface westerlies is also found under all RCPs except RCP2.6 (Swart and Fyfe, 2012), with largest changes in the Pacific basin (Bracegirdle et al., 2013). In austral summer, ozone recovery offsets changes in GHGs to some extent, with a weak reversal of the jet shift found in the multi-model mean under the low emissions scenario of RCP2.6 (Swart and Fyfe, 2012) and weak or poleward shifts in other RCPs (Swart and Fyfe, 2012; Wilcox et al., 2012). Eyring et al. (2013) note the sensitivity of the CMIP5 SH summertime circulation changes to both the strength of the ozone recovery (simulated by some models interactively) and the rate of GHG increases.

Although the poleward shift of the tropospheric jets are robust across models and *likely* under increased GHGs, the dynamical mechanisms behind these projections are still not completely understood and have been explored in both simple and complex models (Chen et al., 2008; Lim and Simmonds, 2009; Butler et al., 2010). The shifts are associated with a strengthening in the upper tropospheric meridional temperature gradient (Wilcox et al., 2012) and hypotheses for associated changes in planetary wave activity and/or synoptic eddy characteristics that impact on the position of the jet have been put forward (Gerber et al., 2012). Equatorward biases in the position of the SH jet (Section 9.5.3.2), while somewhat improved over similar biases in the CMIP3 models (Kidston and Gerber, 2010) still remain, limiting our confidence in the magnitude of future changes.

In summary, poleward shifts in the mid-latitude jets of about 1 to 2 degrees latitude are *likely* at the end of the 21st century under RCP8.5 in both hemispheres (*medium confidence*) with weaker shifts in the NH and under lower emission scenarios. Ozone recovery will *likely* weaken the GHG-induced changes in the SH extratropical circulation in austral summer.

12.4.4.2 Planetary-Scale Overturning Circulations

Large-scale atmospheric overturning circulations and their interaction with other atmospheric mechanisms are significant in determining tropical climate and regional changes in response to enhanced RF. Observed

Projections of future changes in the water cycle are inextricably connected to changes in the energy cycle (Section 12.4.3) and atmospheric circulation (Section 12.4.4).

Saturation vapour pressure increases with temperature, but projected future changes in the water cycle are far more complex than projected temperature changes. Some regions of the world will be subject to decreases in hydrologic activity while others will be subject to increases. There are important local seasonal differences among the responses of the water cycle to climate change as well.

At first sight, the water cycles simulated by CMIP3/5 models may appear to be inconsistent, particularly at regional scales. Anthropogenic changes to the water cycle are superimposed on complex naturally varying modes of the climate (such as El Niño-Southern Oscillation (ENSO), AO, Pacific Decadal Oscillation (PDO), etc.) aggravating the differences between model projections. However, by careful consideration of the interaction of the water cycle with changes in other aspects of the climate system, the mechanisms of change are revealed, increasing confidence in projections.

12.4.5.1 Atmospheric Humidity

Atmospheric water vapour is the primary GHG in the atmosphere. Its changes affect all parts of the water cycle. However, the amount of water vapour is dominated by naturally occurring processes and not significantly affected directly by human activities. A common experience from past modelling studies is that relative humidity (RH) remains approximately constant on climatological time scales and planetary space scales, implying a strong constraint by the Clausius–Clapeyron relationship on how specific humidity will change. The AR4 stated that 'a broad-scale, quasi-unchanged RH response [to climate change] is uncontroversial' (Randall et al., 2007). However, underlying this fairly straightforward behaviour are changes in RH that can influence changes in cloud cover and atmospheric convection (Sherwood, 2010). More recent analysis provides further detail and insight on RH changes. Analysis of CMIP3 and CMIP5 models shows near-surface RH decreasing over most land areas as temperatures increase with the notable exception of parts of tropical Africa (O'Gorman and Muller, 2010) (Figure 12.21). The prime contributor to these decreases in RH over land is the larger temperature increases over land than over ocean in the RCP scenarios (Joshi et al., 2008; Fasullo, 2010; O'Gorman and Muller, 2010). The specific humidity of air originating over more slowly warming oceans will be governed by saturation temperatures of oceanic air. As this air moves over land and is warmed, its relative humidity drops as any further moistening of the air over land is insufficient to maintain constant RH, a behaviour Sherwood et al. (2010) term a last-saturation-temperature constraint. The RH decrease over most land areas by the end of the 21st century is consistent with a last-saturation-temperature constraint and with observed behaviour during the first decade of the current century (Section 2.5.5; Simmons et al., 2010). Land–ocean differences in warming are projected to continue through the 21st century, and although the CMIP5 projected changes are small, they are consistent with a last-saturation constraint, indicating with *medium confidence* that reductions in near-surface RH over many land areas are *likely*.

12.4.5.2 Patterns of Projected Average Precipitation Changes

Global mean precipitation changes have been presented in Section 12.4.1.1. The processes that govern large-scale changes in precipitation are presented in Section 7.6, and are used here to interpret the

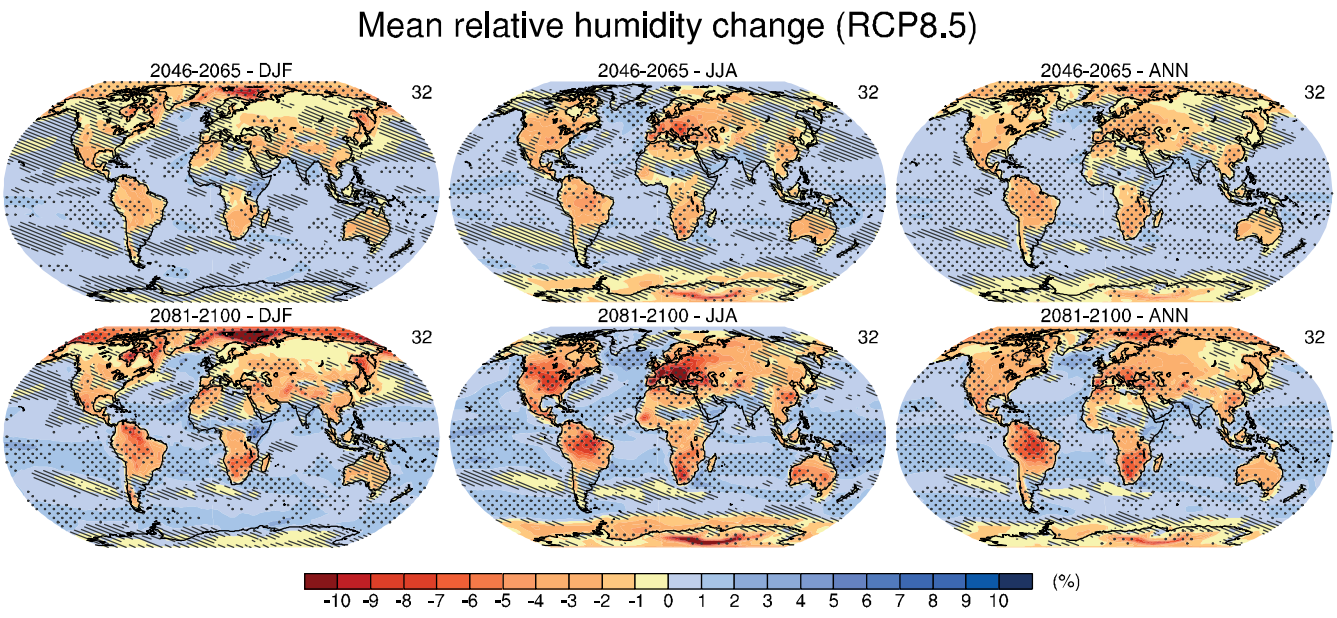

Figure 12.21 | Projected changes in near-surface relative humidity from the CMIP5 models under RCP8.5 for the December, January and February (DJF, left), June, July and August (JJA, middle) and annual mean (ANN, right) averages relative to 1986–2005 for the periods 2046–2065 (top row), 2081–2100 (bottom row). The changes are differences in relative humidity percentage (as opposed to a fractional or relative change). Hatching indicates regions where the multi-model mean change is less than one standard deviation of internal variability. Stippling indicates regions where the multi-model mean change is greater than two standard deviations of internal variability and where at least 90% of models agree on the sign of change (see Box 12.1).

agreement between models is the smallest (Chou et al., 2009; Allan, 2012). A robust feature is the decline of precipitation on the poleward flanks of the subtropical dry zones as a consequence of the Hadley Cell expansion, with possible additional decrease from a poleward shift of the mid latitude storm tracks (Seager et al., 2010; Scheff and Frierson, 2012). On seasonal time scales, the minimum and the maximum values of precipitation both increase, with a larger increase of the maximum and therefore an increase of the annual precipitation range (Sobel and Camargo, 2011; Chou and Lan, 2012).

Long-term precipitation changes are driven mainly by the increase of the surface temperature, as presented above, but other factors also contribute to them. Recent studies suggest that CO_2 increase has a significant direct influence on atmospheric circulation, and therefore on global and tropical precipitation changes (Andrews et al., 2010; Bala et al., 2010; Cao et al., 2012; Bony et al., 2013). Over the ocean, the positive RF from increased atmospheric CO_2 reduces the radiative cooling of the troposphere and the large scale rising motion and hence reduces precipitation in the convective regions. Over large landmasses, the direct effect of CO_2 on precipitation is the opposite owing to the small thermal inertia of land surfaces (Andrews et al., 2010; Bala et al., 2010; Cao et al., 2012; Bony et al., 2013). Regional precipitation changes are also influenced by aerosol and ozone (Ramanathan et al., 2001; Allen et al., 2012; Shindell et al., 2013a) through both local and large-scale processes, including changes in the circulation. Stratospheric ozone depletion contributes to the poleward expansion of the Hadley Cell and the related change of precipitation in the SH (Kang et al., 2011) whereas black carbon and tropospheric ozone increases are major contributors in the NH (Allen et al., 2012). Regional precipitation changes depend on regional forcings and on how models simulate their local and remote effects. Based on CMIP3 results, the inter-model spread of the estimate of precipitation changes over land is larger than the inter-scenario spread except in East Asia (Frieler et al., 2012).

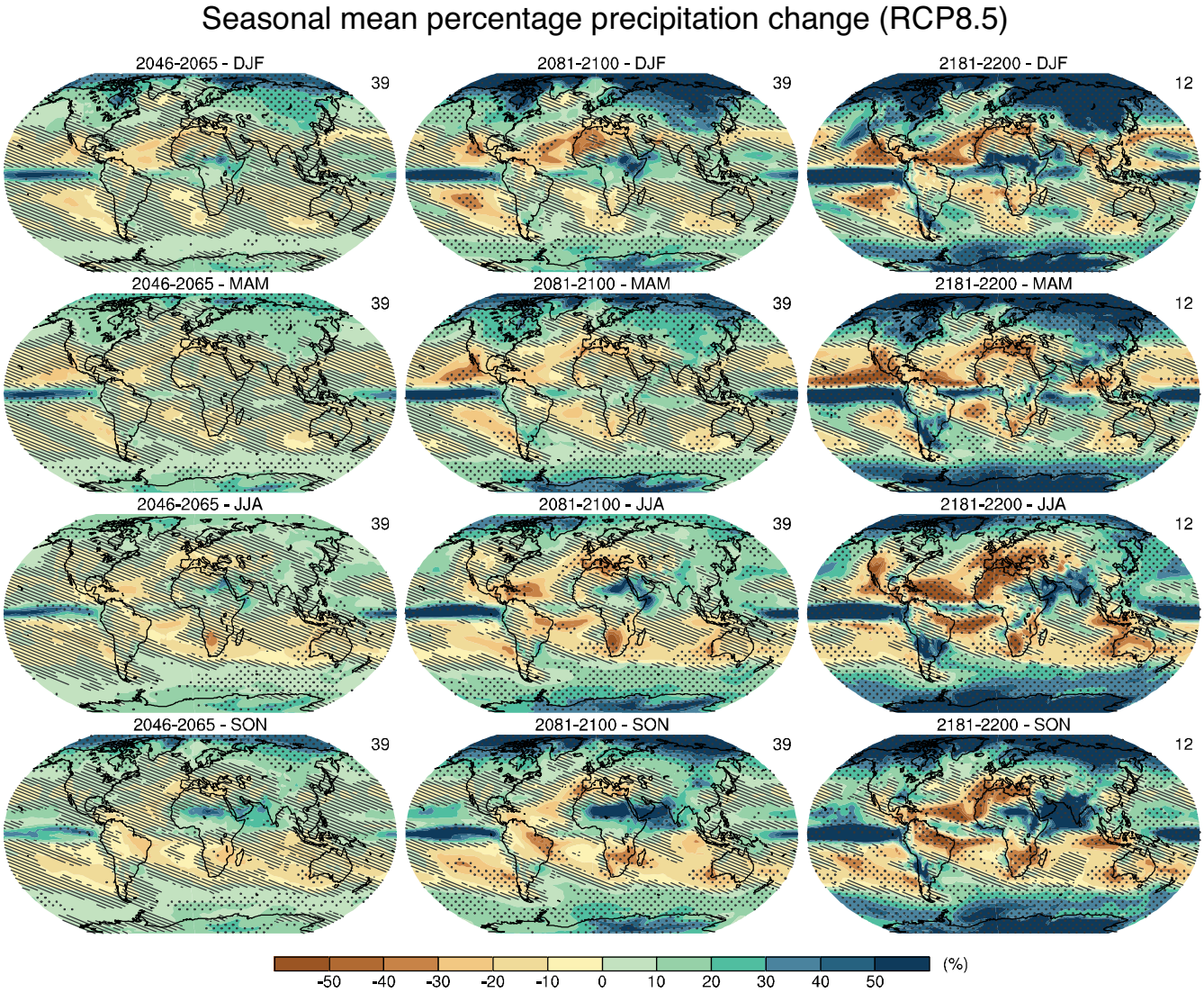

Figure 12.22 | Multi-model CMIP5 average percentage change in seasonal mean precipitation relative to the reference period 1986–2005 averaged over the periods 2045–2065, 2081–2100 and 2181–2200 under the RCP8.5 forcing scenario. Hatching indicates regions where the multi-model mean change is less than one standard deviation of internal variability. Stippling indicates regions where the multi-model mean change is greater than two standard deviations of internal variability and where at least 90% of models agree on the sign of change (see Box 12.1).

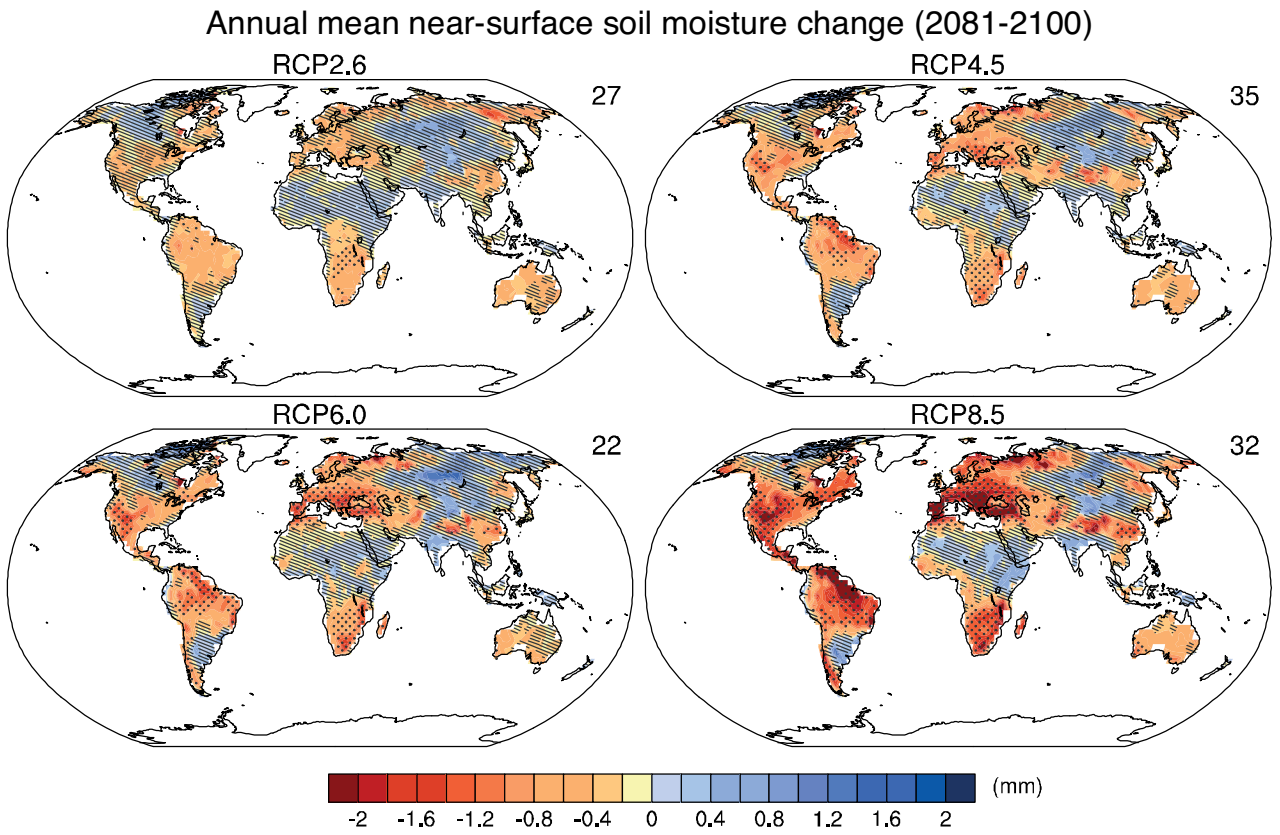

Figure 12.23 | Change in annual mean soil moisture (mass of water in all phases in the uppermost 10 cm of the soil) (mm) relative to the reference period 1986–2005 projected for 2081–2100 from the CMIP5 ensemble. Hatching indicates regions where the multi-model mean change is less than one standard deviation of internal variability. Stippling indicates regions where the multi-model mean change is greater than two standard deviations of internal variability and where at least 90% of models agree on the sign of change (see Box 12.1). The number of CMIP5 models used is indicated in the upper right corner of each panel.

projected widening of the Hadley Circulation that shifts downwelling, thus inhibiting precipitation in these regions. The large-scale drying in the Mediterranean, southwest USA, and southern Africa appear across generations of projections and climate models and is deemed *likely* as global temperatures rise and will increase the risk of agricultural drought. In addition, an analysis of CMIP3 and CMIP5 projections of soil moisture in five drought-prone regions indicates that the differences in future forcing scenarios are the largest source of uncertainty in such regions rather than differences between model responses (Orlowsky and Seneviratne, 2012).

Other recent assessments include multi-model ensemble approaches, dynamical downscaling, and regional climate models applied around the globe and illustrate the variety of issues influencing soil moisture changes. Analyses of the southwestern USA using CMIP3 models (Christensen and Lettenmaier, 2007; Seager et al., 2007) show consistent projections of drying, primarily due to a decrease in winter precipitation. In contrast, Kellomaki et al. (2010) find that SRES A2 projections for Finland yield decreased snow depth, but soil moisture generally increases, consistent with the general increase in precipitation occurring in high northern latitudes. Kolomyts and Surova (2010), using projections from the CMIP3 models, GISS and HadCM2, under the SRES A2 forcing, show that vegetation type has substantial influence on the development of pronounced drying over the 21st century in Middle Volga Region forests.

Projected changes in soil moisture from the CMIP3/5 models also show substantial seasonal variation. For example, soil moisture changes in the North American midlatitudes, coupled with projected warming, increases the strength of land–atmosphere coupling during spring and summer in 15 GCMs under RCP8.5 (Dirmeyer et al., 2013). For the Cline River watershed in western Canada, Kienzle et al. (2012) find decreases in summer soil moisture content, but annual increases averaging 2.6% by the 2080s using a suite of CMIP3 GCMs simulating B1, A1B and A2 scenarios to drive a regional hydrology model. Hansen et al. (2007), using dynamical downscaling of one GCM running the A2 scenario, find summer soil moisture decreases in Mongolia of up to 6% due to increased potential evaporation in a warming climate and decreased precipitation and decreased precipitation.

Soil moisture projections in high latitude permafrost regions are critically important for assessing future climate feedbacks from trace-gas emissions (Zhuang et al., 2004; Riley et al., 2011) and vegetation changes (Chapin et al., 2005). In addition to changes in precipitation, snow cover and evapotranspiration, future changes in high-latitude soil moisture also will depend on permafrost degradation, thermokarst evolution, rapid changes in drainage (Smith et al., 2005), and changes in plant communities and their water demands. Current understanding of these interacting processes at scales relevant to climate is poor, so that full incorporation in current GCMs is lacking.

12.4.5.4 Runoff and Evaporation

In the AR4, 21st century model-projected runoff consistently showed decreases in southern Europe, the Middle East, and southwestern USA and increases in Southeast Asia, tropical East Africa and at high northern latitudes. The same general features appear in the CMIP5 ensemble of GCMs for all four RCPs shown in Figure 12.24, with the areas of most robust change typically increasing with magnitude of forcing change. However, the robustness of runoff decreases in the southwestern USA is less in the CMIP5 models compared to the AR4. The large decreases in runoff in southern Europe and southern Africa are consistent with changes in the Hadley Circulation and related precipitation decreases and warming-induced evapotranspiration increases. The high northern latitude runoff increases are *likely* under RCP8.5 and consistent with the projected precipitation increases (Figure 12.22). The consistency of changes across different generations of models and different forcing scenarios, together with the physical consistency of change indicates that decreases are also *likely* in runoff in southern Europe, the Middle East, and southern Africa in this scenario.

A number of reports since the AR4 have updated findings from CMIP3 models and analyzed a large set of mechanisms affecting runoff. Several studies have focussed on the Colorado River basin in the United States (Christensen and Lettenmaier, 2007; McCabe and Wolock, 2007; Barnett and Pierce, 2008; Barnett et al., 2008) showing that runoff reductions that do happen under global warming occur through a combination of evapotranspiration increases and precipitation decreases, with the overall reduction in river flow exacerbated by human water demands on the basin's supply.

A number of CMIP3 analyses have examined trends and seasonal shifts in runoff. For example, Kienzle et al. (2012) studied climate change scenarios over the Cline River watershed in western Canada and projected (1) spring runoff and peak streamflow up to 4 weeks earlier than in 1961–1990; (2) significantly higher streamflow between October and June; and (3) lower streamflow between July and September. For the Mediterranean basin, an ensemble of regional climate models driven by several GCMs using the A1B scenario have a robust decrease in runoff emerging only after 2050 (Sanchez-Gomez et al., 2009).

Annual mean surface evaporation in the models assessed in AR4 showed increases over most of the ocean and increases or decreases over land with largely the same pattern over land as increases and decreases in precipitation. Similar behaviour occurs in an ensemble of CMIP5 models (Figure 12.25). Evaporation increases over most of the ocean and land, with prominent areas of decrease over land occurring in southern Africa and northwestern Africa along the Mediterranean. The areas of decrease correspond to areas with reduced precipitation. There is some uncertainty about storm-track changes over Europe (see Sections 12.4.3 and 14.6.2). However, the consistency of the decreases across different generations of models and different forcing scenarios along with the physical basis for the precipitation decrease

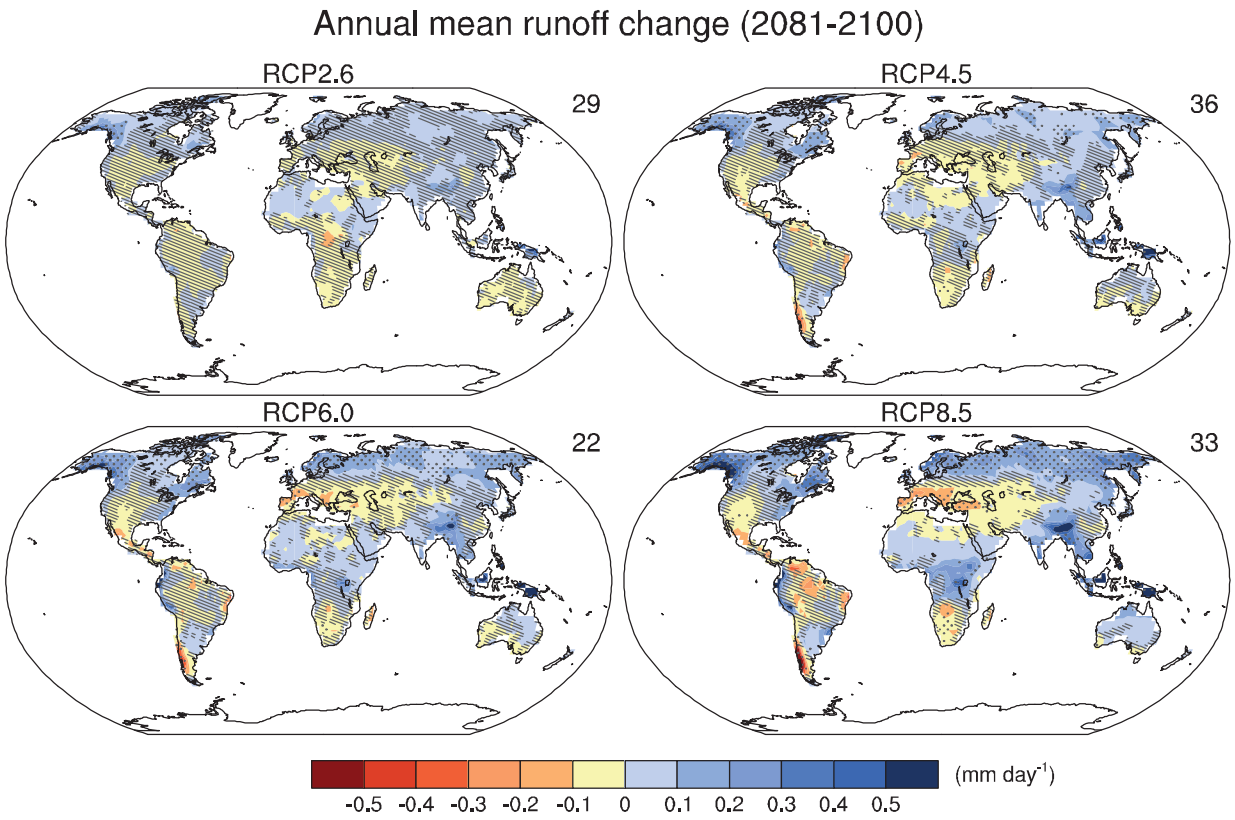

Figure 12.24 | Change in annual mean runoff relative to the reference period 1986–2005 projected for 2081–2100 from the CMIP5 ensemble. Hatching indicates regions where the multi-model mean change is less than one standard deviation of internal variability. Stippling indicates regions where the multi-model mean change is greater than two standard deviations of internal variability and where at least 90% of models agree on the sign of change (see Box 12.1). The number of CMIP5 models used is indicated in the upper right corner of each panel.

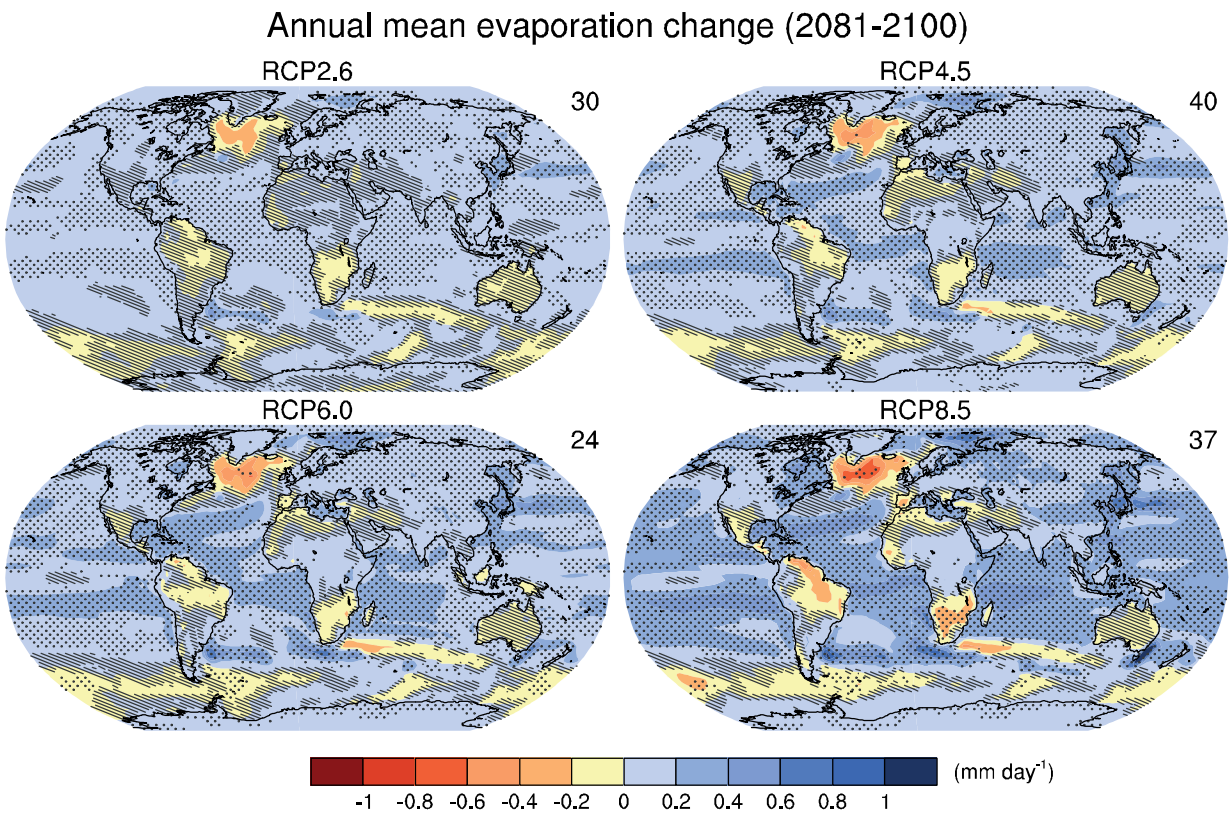

Figure 12.25 | Change in annual mean evaporation relative to the reference period 1986–2005 projected for 2081–2100 from the CMIP5 ensemble. Hatching indicates regions where the multi-model mean change is less than one standard deviation of internal variability. Stippling indicates regions where the multi-model mean change is greater than two standard deviations of internal variability and where at least 90% of models agree on the sign of change (see Box 12.1). The number of CMIP5 models used is indicated in the upper right corner of each panel.

indicates that these decreases in annual mean evaporation are *likely* under RCP8.5, but with *medium confidence*. Annual mean evaporation increases over land in the northern high latitudes are consistent with the increase in precipitation and the overall warming that would increase potential evaporation. For the northern high latitudes, the physical consistency and the similar behaviour across multiple generations and forcing scenarios indicates that annual mean evaporation increases there are *likely*, with *high confidence*.

Evapotranspiration changes partly reflect changes in precipitation. However, some changes might come from altered biological processes. For example, increased atmospheric CO_2 promotes stomatal closure and reduced transpiration (Betts et al., 2007; Cruz et al., 2010) which can potentially yield increased runoff. There is potential for substantial feedback between vegetation changes and regional water cycles, though the impact of such feedback remains uncertain at this point due to limitations on modelling crop and other vegetation processes in GCMs (e.g., Newlands et al., 2012) and uncertainties in plant response, ecosystem shifts and land management changes.

12.4.5.5 Extreme Events in the Water Cycle

In addition to the changes in the seasonal pattern of mean precipitation described above, the distribution of precipitation events is projected to undergo profound changes (Gutowski et al., 2007; Sun et al., 2007; Boberg et al., 2010). At daily to weekly scales, a shift to more intense individual storms and fewer weak storms is projected (Seneviratne et al., 2012). At seasonal or longer time scales, increased evapotranspiration over land can lead to more frequent and more intense periods of agricultural drought.

A general relationship between changes in total precipitation and extreme precipitation does not exist (Seneviratne et al., 2012). Two possible mechanisms controlling short-term extreme precipitation amounts are discussed at length in the literature and are similar to the thermodynamic and dynamical mechanisms detailed above for changes in average precipitation.

The first considers that extreme precipitation events occur when most of the available atmospheric water vapour rapidly precipitates out in a single storm. The maximum amount of water vapour in air (saturation) is determined by the Clausius–Clapeyron relationship. As air temperature increases, this saturated amount of water also increases (Allen and Ingram, 2002; Pall et al., 2007; Allan and Soden, 2008; Kendon et al., 2010). Kunkel et al. (2013) examined the CMIP5 model RCP4.5 and 8.5 projections for changes in maximum water vapour concentrations, a principal factor controlling the probable bound on maximum precipitation, concluding that maximum water vapour changes are comparable to mean water vapour changes but that the potential for changes in dynamical factors is less compelling. Such increases in atmospheric water vapour are expected to increase the intensity of individual precipitation events, but have less impact on their frequency. As a result

projected increases in extreme precipitation may be more reliable than similar projections of changes in mean precipitation in some regions (Kendon et al., 2010).

A second mechanism for extreme precipitation put forth by O'Gorman and Schneider (2009a, 2009b) is that such events are controlled by anomalous horizontal moisture flux convergence and associated convective updrafts which would change in a more complicated fashion in a warmer world (Sugiyama et al., 2010). Emori and Brown (2005) showed that the thermodynamic mechanism dominated over the dynamical mechanism nearly everywhere outside the tropical warm pool. However, Utsumi et al. (2011) used gridded observed daily data to find that daily extreme precipitation monotonically increases with temperature only at high latitudes, with the opposite behaviour in the tropics and a mix in the mid-latitudes. Li et al. (2011a) found that both mechanisms contribute to extreme precipitation in a high-resolution aquaplanet model with updrafts as the controlling element in the tropics and air temperature controlling the mid-latitudes consistent with the results by Chou et al. (2012). Using a high-resolution regional model, Berg et al. (2009) found a seasonal dependence in Europe with the Clausius–Clapeyron relationship providing an upper limit to daily precipitation intensity in winter but water availability rather than storage capacity is the controlling factor in summer. Additionally, Lenderink and Van Meijgaard (2008) found that very short (sub-daily) extreme precipitation events increase at a rate twice the amount predicted by Clausius–Clapeyron scaling in a very high-resolution model over Europe suggesting that both mechanisms can interact jointly. Gastineau and Soden (2009) found in the CMIP3 models that the updrafts associated with the most extreme tropical precipitation events actually weaken despite an increase in the frequency of the heaviest rain rates further complicating simple mechanistic explanations. See also Sections 7.6.5 and 11.3.2.5.2.

Projections of changes in future extreme precipitation may be larger at the regional scales than for future mean precipitation, but natural variability is also larger causing a tendency for signal-to-noise ratios to decrease when considering increasingly extreme metrics. However, mechanisms of natural variability still are a large factor in assessing the robustness of projections (Kendon et al., 2008). In addition, large-scale circulation changes, which are uncertain, could dominate over the above mechanisms depending on the rarity and type of events considered. However, analysis of CMIP3 models suggests circulation changes are potentially insufficient to offset the influence of increasing atmospheric water vapour on extreme precipitation change over Europe at least on large spatial scales (Kendon et al., 2010). An additional shift of the storm track has been shown in models with a better representation of the stratosphere, and this is found to lead to an enhanced increase in extreme rainfall over Europe in winter (Scaife et al., 2012).

Similar to temperature extremes (Section 12.4.3.3), the definition of a precipitation extreme depends very much on context and is often used in discussion of particular climate-related impacts (Seneviratne et al. (2012), Box 3.1). Consistently, climate models project future episodes of more intense precipitation in the wet seasons for most of the land areas, especially in the NH and its higher latitudes, and the monsoon regions of the world, and at a global average scale. The actual magnitude of the projected change is dependent on the model used,

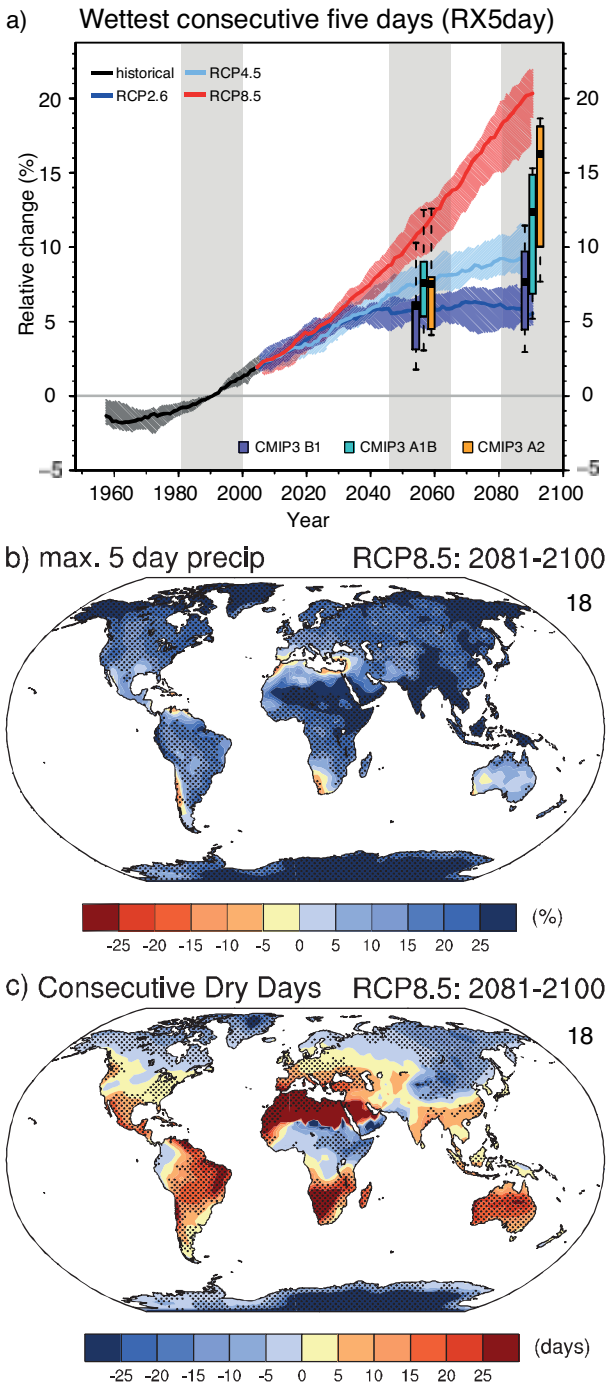

Figure 12.26 | (a, b) Projected percent changes (relative to the 1981–2000 reference period in common with CMIP3) from the CMIP5 models in RX5day, the annual maximum five-day precipitation accumulation. (a) Global average percent change over land regions for the RCP2.6, RCP4.5 and RCP8.5 scenarios. Shading in the time series represents the interquartile ensemble spread (25th and 75th quantiles). The box-and-whisker plots show the interquartile ensemble spread (box) and outliers (whiskers) for 11 CMIP3 model simulations of the SRES scenarios A2 (orange), A1B (cyan) and B1 (purple) globally averaged over the respective future time periods (2046–2065 and 2081–2100) as anomalies from the 1981–2000 reference period. (b) Percent change over the 2081–2100 period in the RCP8.5 scenario. (c) Projected change in annual CDD, the maximum number of consecutive dry days when precipitation is less than 1 mm, over the 2081–2100 period in the RCP8.5 scenario (relative to the 1981–2000 reference period) from the CMIP5 models. Stippling indicates gridpoints with changes that are significant at the 5% level using a Wilcoxon signed-ranked test. (Updated from Sillmann et al. (2013), excluding the FGOALS-s2 model.)

warming) (Kay et al., 2011; Winton, 2011; Mahlstein and Knutti, 2012). This sensitivity may be crucial for determining future sea ice losses. Indeed, a clear relationship exists at longer than decadal time scales in climate change simulations between the annual mean or September mean Arctic sea ice extent and the annual mean global surface temperature change for ice extents larger than ~1 × 10^6 km^2 (e.g., Ridley et al., 2007; Zhang, 2010b; NRC, 2011; Winton, 2011; Mahlstein and Knutti, 2012). This relationship is illustrated in Figure 12.30 for both CMIP3 and CMIP5 models. From this figure, it can be seen that the sea ice sensitivity varies significantly from model to model and is generally larger and in better agreement among models in CMIP5.

A complete and detailed explanation for what controls the range of Arctic sea ice responses in models over the 21st century remains elusive, but the Arctic sea ice provides an example where process-based constraints can be used to reduce the spread of model projections (Overland et al., 2011; Collins et al., 2012; Hodson et al., 2012). For CMIP3 models, results indicate that the changes in Arctic sea ice mass budget over the 21st century are related to the late 20th century mean sea ice thickness distribution (Holland et al., 2010), average sea ice thickness (Bitz, 2008; Hodson et al., 2012), fraction of thin ice cover (Boé et al., 2009b) and oceanic heat transport to the Arctic (Mahlstein and Knutti, 2011). For CMIP5 models, Massonnet et al. (2012) showed that the time needed for the September Arctic sea ice areal coverage to drop below a certain threshold is highly correlated with the September sea ice extent and annual mean sea ice volume averaged over the past several decades (Figure 12.31a, b). The timing of a seasonally ice-free Arctic Ocean or the fraction of remaining sea ice in September at any time during the 21st century were also found to correlate with the past trend in September Arctic sea ice extent and the amplitude of the mean seasonal cycle of sea ice extent (Boé et al., 2009b; Collins et al., 2012; Massonnet et al., 2012) (Figure 12.31c, d). All these empirical

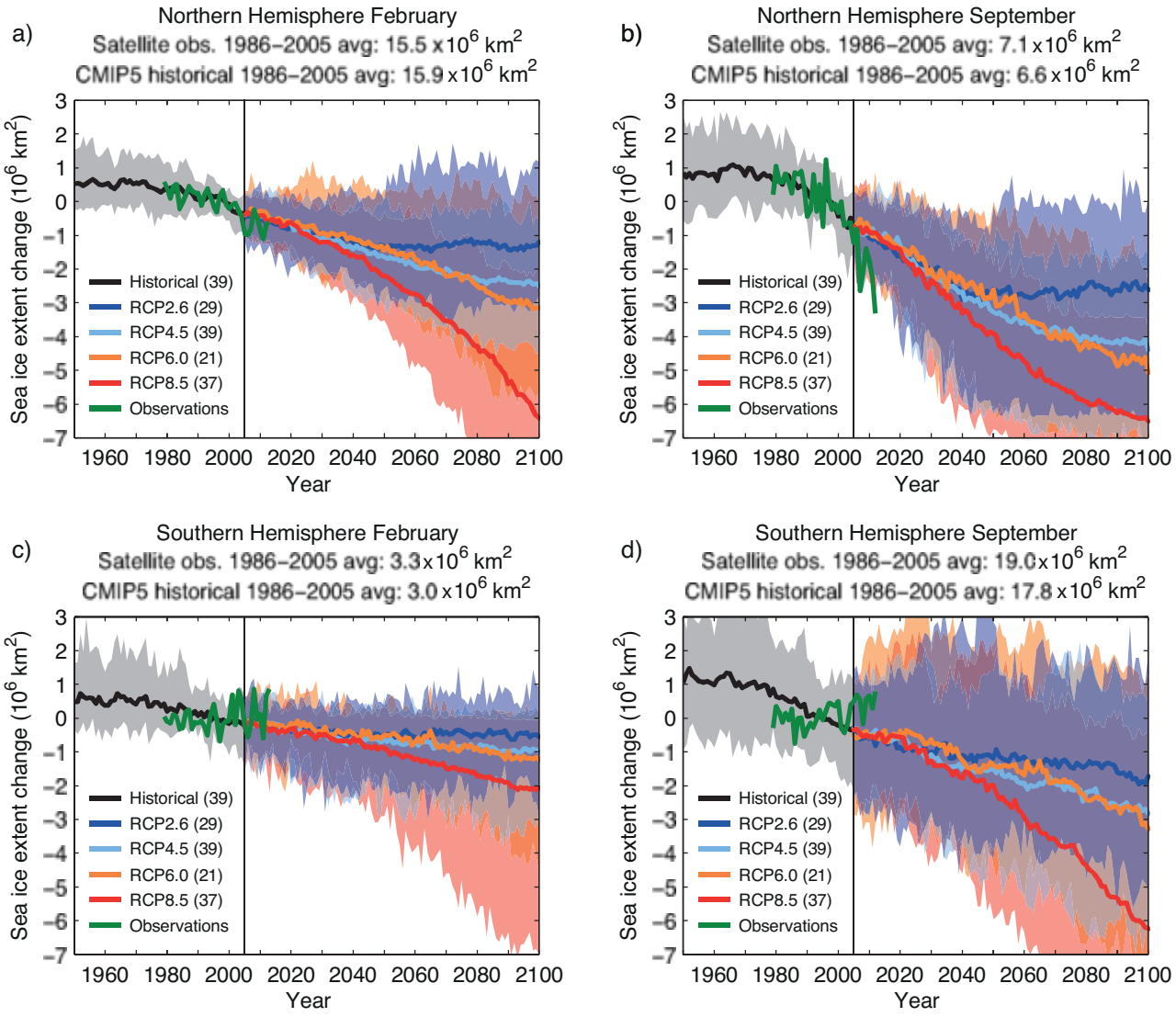

Figure 12.28 | Changes in sea ice extent as simulated by CMIP5 models over the second half of the 20th century and the whole 21st century under RCP2.6, RCP4.5, RCP6.0 and RCP8.5 for (a) Northern Hemisphere February, (b) Northern Hemisphere September, (c) Southern Hemisphere February and (d) Southern Hemisphere September. The solid curves show the multi-model means and the shading denotes the 5 to 95% range of the ensemble. The vertical line marks the end of CMIP5 historical climate change simulations. One ensemble member per model is taken into account in the analysis. Sea ice extent is defined as the total ocean area where sea ice concentration exceeds 15% and is calculated on the original model grids. Changes are relative to the reference period 1986–2005. The number of models available for each RCP is given in the legend. Also plotted (solid green curves) are the satellite data of Comiso and Nishio (2008, updated 2012) over 1979–2012.

relationships can be understood on simple physical grounds (see the aforementioned references for details).

These results lend support for weighting/recalibrating the models based on their present-day Arctic sea ice simulations. Today, the optimal approach for constraining sea ice projections from climate models is unclear, although one notes that these methods should have a credible underlying physical basis in order to increase confidence in their results (see Section 12.2). In addition, they should account for the potentially large imprint of natural variability on both observations and model simulations when these two sources of information are to be compared (see Section 9.8.3). This latter point is particularly critical if the past sea ice trend or sensitivity is used in performance metrics given the relatively short observational period (Kay et al., 2011; Overland et al., 2011; Mahlstein and Knutti, 2012; Massonnet et al., 2012; Stroeve et al., 2012). A number of studies have applied such metrics to the CMIP3 and CMIP5 models. Stroeve et al. (2007) and Stroeve et al. (2012) rejected several CMIP3 and CMIP5 models, respectively, on

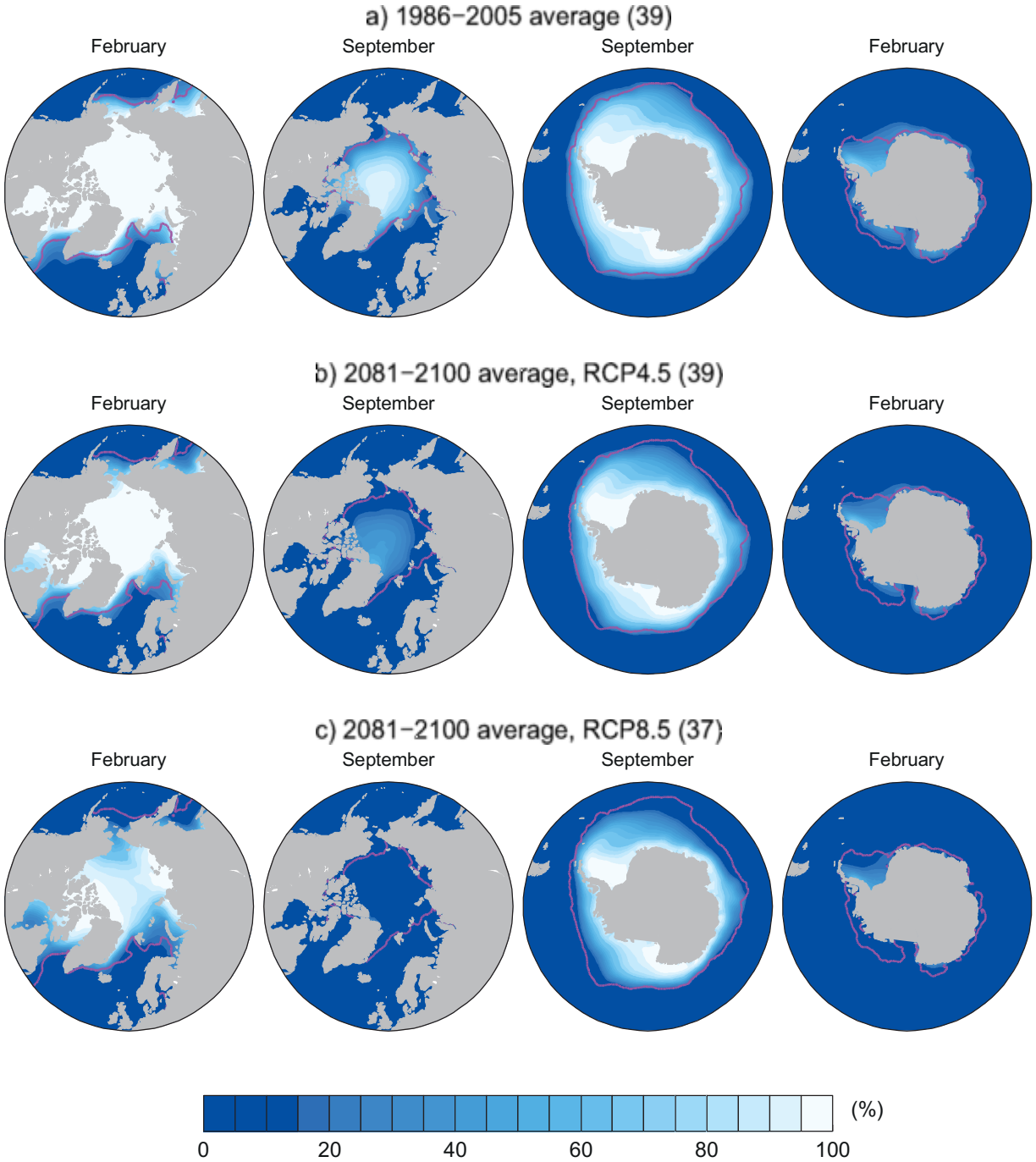

Figure 12.29 | February and September CMIP5 multi-model mean sea ice concentrations (%) in the Northern and Southern Hemispheres for the periods (a) 1986–2005, (b) 2081–2100 under RCP4.5 and (c) 2081–2100 under RCP8.5. The model sea ice concentrations are interpolated onto a 1° × 1° regular grid. One ensemble member per model is taken into account in the analysis, and the multi-model mean sea ice concentration is shown where it is larger than 15%. The number of models available for each RCP is given in parentheses. The pink lines indicate the observed 15% sea ice concentration limits averaged over 1986–2005 (Comiso and Nishio, 2008, updated 2012).

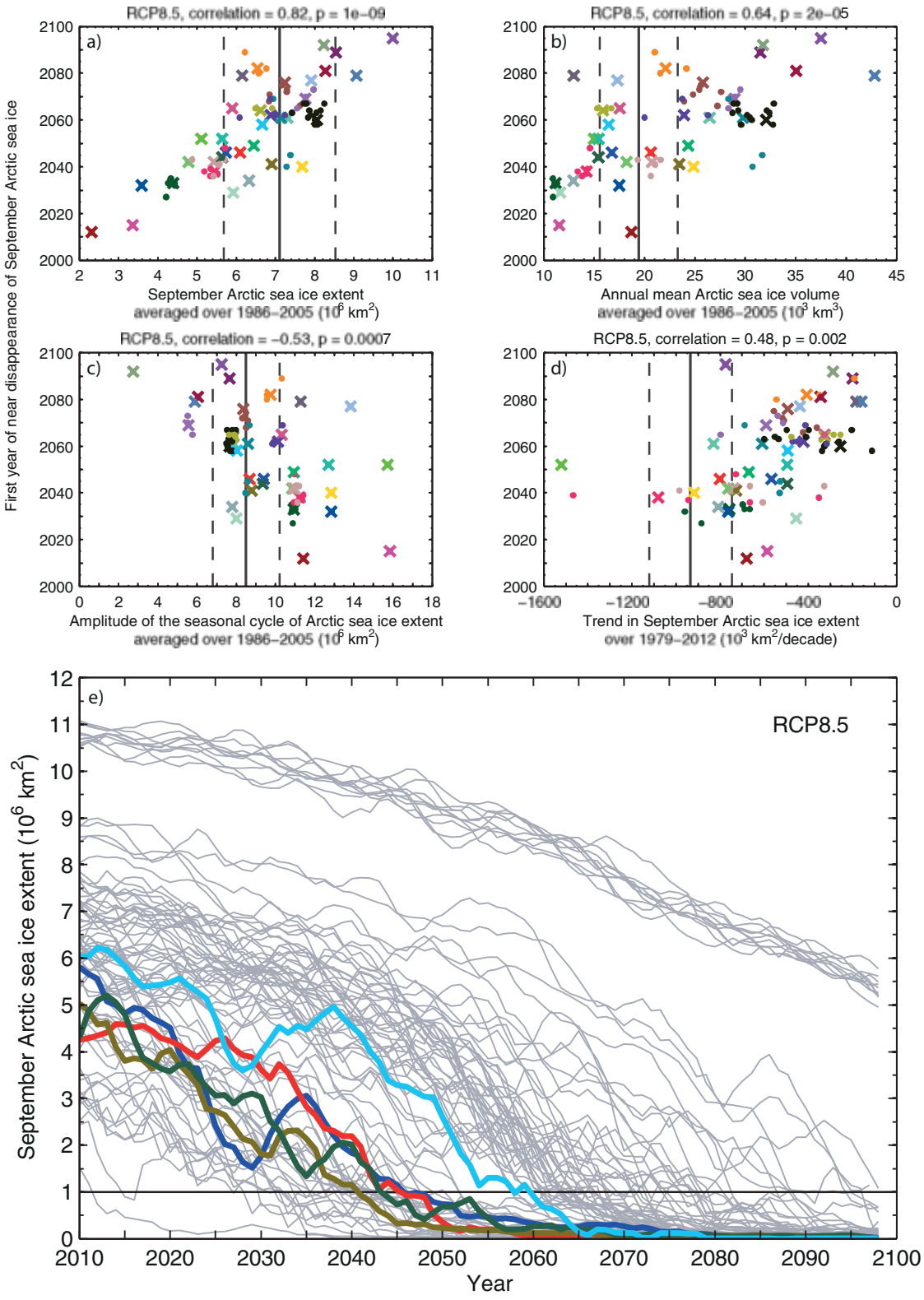

Figure 12.31 | (a–d) First year during which the September Arctic sea ice extent falls below 1 × 10^6 km^2 in CMIP5 climate projections (37 models, RCP8.5) as a function of (a) the September Arctic sea ice extent averaged over 1986–2005, (b) the annual mean Arctic sea ice volume averaged over 1986–2005, (c) the amplitude of the 1986–2005 mean seasonal cycle of Arctic sea ice extent and (d) the trend in September Arctic sea ice extent over 1979–2012. The sea ice diagnostics displayed are calculated on the original model grids. The correlations and one-tailed *p*-values are computed from the multi-member means for models with several ensemble members (coloured crosses), but the ensemble members of individual models are also depicted (coloured dots). The vertical solid and dashed lines show the corresponding observations or bias-adjusted PIOMAS (Pan-Arctic Ice-Ocean Modelling and Assimilation System) reanalysis data (a, c and d: Comiso and Nishio, 2008, updated 2012; b: Schweiger et al., 2011) and the ±20% interval around these data, respectively. (e) Time series of September Arctic sea ice extent (5-year running mean) as simulated by all CMIP5 models and their ensemble members under RCP8.5 (thin curves). The thick, coloured curves correspond to a subset of five CMIP5 models selected on the basis of panels a–d following Massonnet et al. (2012) (see text for details). Note that each of these models provides only one ensemble member for RCP8.5.

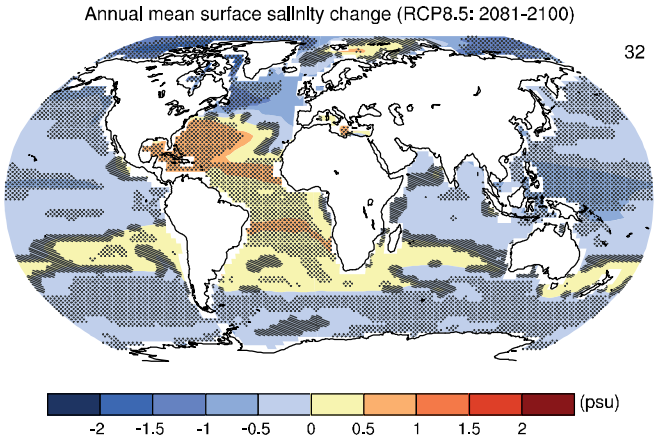

Figure 12.34 | Projected sea surface salinity differences 2081–2100 for RCP8.5 relative to 1986–2005 from CMIP5 models. Hatching indicates regions where the multi-model mean change is less than one standard deviation of internal variability. Stippling indicates regions where the multi-model mean change is greater than two standard deviations of internal variability and where at least 90% of the models agree on the sign of change (see Box 12.1). The number of CMIP5 models used is indicated in the upper right corner.

Durack and Wijffels (2010) and Durack et al. (2012) examined trends in global sea surface salinity (SSS) changes over the period 1950–2008. Their analysis revealed strong, spatially coherent trends in SSS over much of the global ocean, with a pattern that bears striking resemblance to the climatological SSS field and is associated with an intensification of the global water cycle (see Sections 3.3.2.1, 10.4.2 and 12.4.5). The CMIP5 climate model projections available suggest that high SSS subtropical regions that are dominated by net evaporation are typically getting more saline; lower SSS regions at high latitudes are typically getting fresher. They also suggest a continuation of this trend in the Atlantic where subtropical surface waters become more saline as the century progresses (Figure 12.34) (see also Terray et al., 2012). At the same time, the North Pacific is projected to become less saline.

12.4.7.2 Atlantic Meridional Overturning

Almost all climate model projections reveal an increase of high latitude temperature and high latitude precipitation (Meehl et al., 2007b). Both of these effects tend to make the high latitude surface waters lighter and hence increase their stability. As seen in Figure 12.35, all models show a weakening of the AMOC over the course of the 21st century (see Section 12.5.5.2 for further analysis). Projected changes in the strength of the AMOC at high latitudes appear stronger in Geophysical Fluid Dynamics Laboratory (GFDL) CM2.1 when density is used as a vertical coordinate instead of depth (Zhang, 2010a). Once the RF is stabilized, the AMOC recovers, but in some models to less than its pre-industrial level. The recovery may include a significant overshoot (i.e., a weaker circulation may persist) if the anthropogenic RF is eliminated (Wu et al., 2011a). Gregory et al. (2005) found that for all eleven models

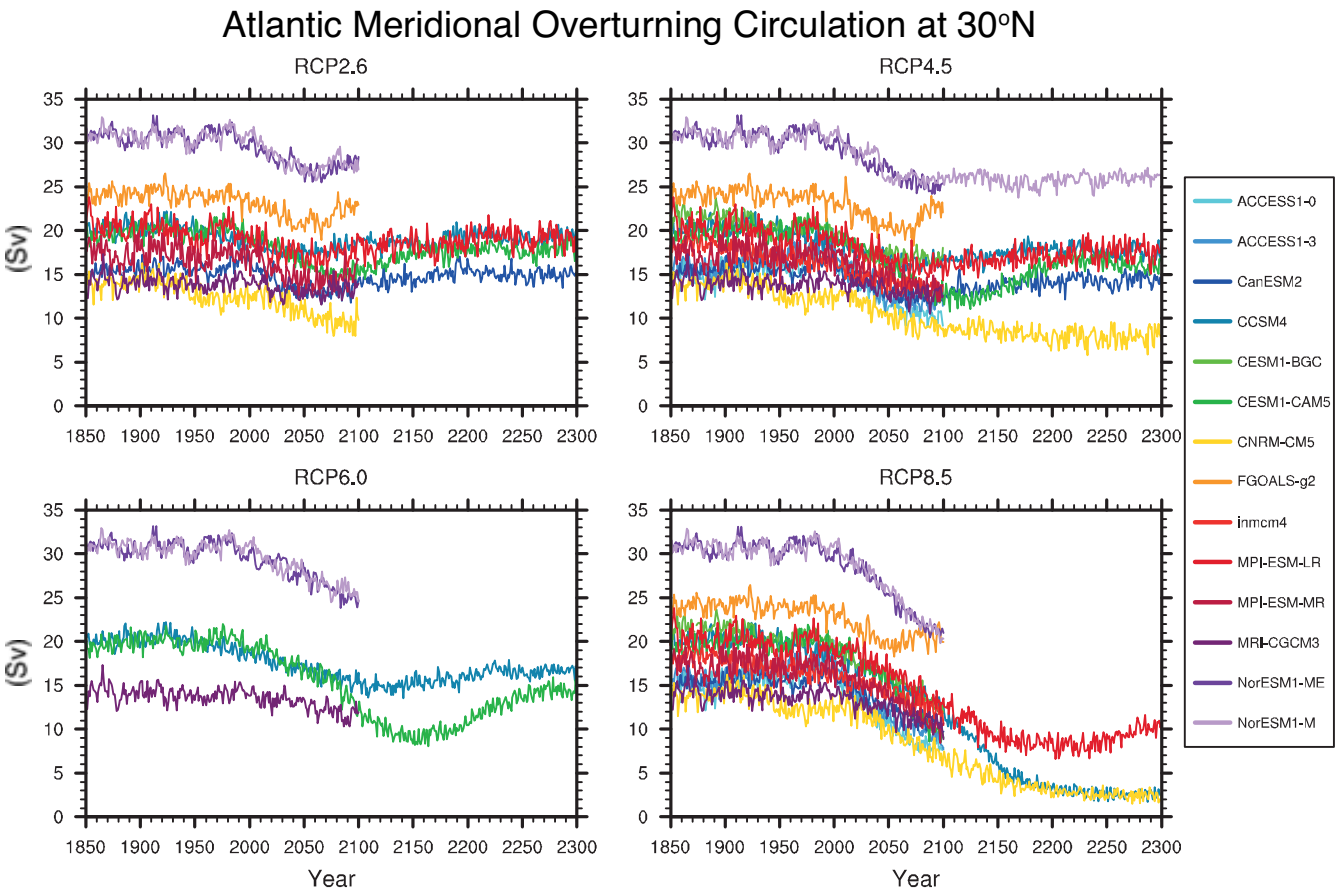

Figure 12.35 | Multi-model projections of Atlantic Meridional Overturning Circulation (AMOC) strength at 30°N from 1850 through to the end of the RCP extensions. Results are based on a small number of CMIP5 models available. Curves show results from only the first member of the submitted ensemble of experiments.